Journal of
Synchrotron Radiation

ISSN 0909-0495

Received 3 April 2009
Accepted 14 August 2009

I18 – the microfocus spectroscopy beamline at the Diamond Light Source

J. Frederick W. Mosselmans,[a]* Paul D. Quinn,[a] Andrew J. Dent,[a] Stuart A. Cavill,[a] Sofia Diaz Moreno,[a] Andrew Peach,[a] Peter J. Leicester,[a] Stephen J. Keylock,[a] Simon R. Gregory,[b] Kirk D. Atkinson[a] and Josep Roque Rosell[a]

[a]Diamond Light Source Ltd, Diamond House, Harwell Science and Innovation Campus, Didcot, Oxfordshire OX11 0DE, UK, and [b]STFC Daresbury Laboratory, Daresbury Science and Innovation Campus, Warrington WA4 4AD, UK. E-mail: fred.mosselmans@diamond.ac.uk

The design and performance of the microfocus spectroscopy beamline at the Diamond Light Source are described. The beamline is based on a 27 mm-period undulator to give an operable energy range between 2 and 20.7 keV, enabling it to cover the *K*-edges of the elements from P to Mo and the L_3-edges from Sr to Pu. Micro-X-ray fluorescence, micro-EXAFS and micro-X-ray diffraction have all been achieved on the beamline with a spot size of $\sim$3 μm. The principal optical elements of the beamline consist of a toroid mirror, a liquid-nitrogen-cooled double-crystal monochromator and a pair of bimorph Kirkpatrick–Baez mirrors. The performance of the optics is compared with theoretical values and a few of the early experimental results are summarized.

Keywords: microfocus; EXAFS; Diamond; XANES; X-ray fluorescence.

1. Introduction

The Diamond Light Source is a 3 GeV third-generation storage ring, and is the UK's new national synchrotron facility. It is the successor to the Synchrotron Radiation Source at Daresbury and opened for users in 2007 (Walker & Fletcher, 2007). The synchrotron is a 24-cell machine with provision for about 40 beamlines. Seven beamlines were opened in early 2007, with a further 15 currently being commissioned or built, such that 22 beamlines will be operating by 2011.

Among the first beamlines opened was the microfocus spectroscopy beamline, I18. I18 takes advantage of the high brightness of the Diamond lattice combined with a 27 mm-period undulator to give an energy-tunable X-ray microbeam with an accessible energy range from 2.0 to 20.7 keV. The beamline is optimized to perform micro-X-ray fluorescence (XRF) mapping studies, micro-X-ray absorption spectroscopy and micro-X-ray diffraction. Microfocus spectroscopy beamlines are becoming increasingly important for the analysis of heterogeneous materials in all fields of science in microscopic detail (*e.g.* Evans, 2006; Flank *et al.*, 2006; Kemner, 2008; Scheidegger *et al.*, 2006). The beamline design and its performance are described in this paper. We also include brief summaries of three of the initial experiments performed on the beamline to demonstrate its capability.

2. The beamline

2.1. Optics

Fig. 1 presents an overview of the optical layout of the beamline. The source is an in-vacuum undulator with a period of 27 mm which was chosen for its performance over the 2–20 keV energy range. The first optical element is a 150 × 75 μrad [horizontal (h) × vertical (v)] cooled aperture used to minimize heat load on the upstream optics by cutting out the off-axis undulator radiation. A set of water-cooled primary

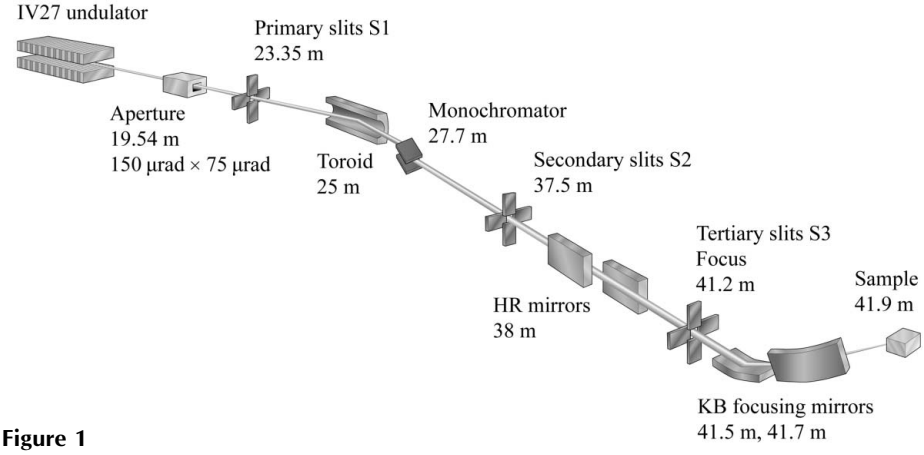

Figure 1
Schematic showing the principal optical elements of the beamline.

slits are used to further define the incoming beam at the entrance of a horizontally deflecting toroidal mirror (Instrument Design Technology) located 25 m from the source. The 1 m-long (0.75 m active area) rhodium-coated silicon mirror is water-cooled and operates at an angle of 3 mrad, which is sufficient to cover the beam footprint given the small horizontal source divergence at Diamond. The toroidal shape is achieved by bending a cylindrical mirror. The mirror collimates the beam in the vertical plane. In the horizontal plane the beam is focused using an elliptical bend onto a set of adjustable slits (secondary slits in Fig. 1), which are located after the monochromator, providing a secondary source for the horizontal focusing optic. Demagnification by a factor of two provides good efficiency at the focus, and collimation removes the influence of vertical source divergence so the energy resolution is primarily a function of the bandpass of the crystals used in the monochromator.

The monochromator (Oxford Danfysik) is a fixed-exit double-crystal design which allows for three pairs of crystals to be positioned in the beam by an in-vacuum translation. Si(111) and Si(311) crystal sets are installed allowing access to photon energies between 2 keV and 20 keV with resolutions of 1.4×10^{-4} and 3×10^{-5} ($\Delta E/E$), respectively. The fixed beam exit is maintained by translating the second crystal vertically. Owing to the high power density of the undulator the first and second crystals are indirectly cooled with liquid nitrogen. Both sets of crystals are mounted over an indium foil onto a copper block, through which liquid nitrogen flows. At these temperatures silicon has negligible thermal expansion and a high thermal conductivity which minimizes any 'thermal bumps'. Diamond now operates in top-up mode, with an injection every ten minutes. This gives rise to a 1% variation in ring current at most, so changes in the heat load during an experiment are largely related to undulator gap and harmonic changes. In order to cover the required energy range the monochromator has an angular range of 80°. To maintain the alignment of the first and second crystal lattice planes over this angular range a coarse motor ($\sim\pm3$ mrad) and a fine piezo actuator ($\sim\pm200$ µrad) allow for pitch and roll adjustments.

Downstream of the monochromator are the secondary slits which, as previously mentioned, define a secondary source for the focusing optics in the horizontal direction. At this point the beam size is 600×140 µm (h × v). The slit position is fixed but the slit width can be controlled *via* a parallelogram mechanism. The secondary slits are used as a beam position monitor. Drain currents are collected from the individual blades and fed back to control the fine pitch and roll piezo actuators of the monochromator to keep the beam centred on the slits. To move over the entire energy range, the coarse roll motor of the monochromator must be adjusted to compensate for errors on the second crystal translation slide. The piezo fine roll motor has the necessary range for movement between 2 keV and 12 keV or between 7 keV and 21 keV, but to move between these energy ranges the coarse motor must be used. This does not affect the focus or beam position. Furthermore, the optimum perpendicular translation of the secondary crystals and undulator gap positions are regularly measured and tabulated. This ensures a fixed position at the sample. The energy reproducibility of the monochromator is good; for example we have measured Ti foil spectra in transmission mode 36 h apart; the shift in pre-edge position was ~0.03 eV (below the resolution of the beamline). However, we have found that the angular calibration of the monochromator needs adjusting by about 0.2° between a calibration at the Mo *K*-edge (20.0 keV) and the S *K*-edge (2.47 keV) for reasons that are not entirely clear. This is a reproducible shift in calibration, and thus not indicative of instability.

Rejection of the higher harmonics in the X-ray beam after the monochromator for energies below 8 keV is accomplished by a pair of horizontally reflecting flat silicon mirrors, which give a constant horizontal beam offset of 3 mm. The mirror has stripes of nickel and rhodium; these are accessed by vertical translation.

Just prior to the vessel containing the final focusing mirrors is a set of slits, which remove scatter in the vertical direction and limit the horizontal beam size onto the horizontally focusing mirror, and are also used in optimizing the beam focus.

The final focusing of the beam is achieved by a Kirkpatrick–Baez (KB) (Kirkpatrick & Baez, 1948) system (Oxford Danfysik). The beam is vertically collimated, and focusing in this direction is achieved using a 200 mm-long (175 mm active area) parabolic mirror; a 150 mm-long (125 mm active area) elliptical mirror is used for horizontal focusing. Control of the mirror shape is achieved using a 'bimorph' adaptive mirror system with eight piezoelectric actuators per mirror (Susini *et al.*, 1995, 1996; Signorato *et al.*, 1998). The mirror substrates are made of fused silica and coated with 8 mm-wide Pt, Pd and Cr stripes and can be operated over a 2–6 mrad angular range allowing the mirror to be used both for focusing and harmonic rejection. The focal spot is located at 425 mm and 225 mm from the centre of the vertical and horizontal mirrors, respectively, which gives a standard working distance of 110 mm between the end of the KB vessel and focal plane under normal conditions. The dynamic range of the mirror allows for the focal point to be adjusted from +75 mm (downstream) to −25 mm (upstream) from this nominal position to accommodate user-supplied sample environments.

The performance of the focusing system is largely determined by the quality of the mirrors, *i.e.* by the intrinsic slope errors and the surface roughness. To determine the requirements of the beamline, optics ray-tracing simulations were performed using the *Shadow* package (Welnak *et al.*, 1994). In order to achieve a 1 µm focus the toroidal mirror should have a r.m.s. surface roughness of less than 3.5 Å and r.m.s. slope errors of no more than 1.5 µrad and 10 µrad in the tangential and sagittal directions, respectively. The toroidal mirror system was delivered with a 2.8 Å r.m.s. surface roughness with r.m.s. slope errors of 0.66 µrad and 2.91 µrad in the tangential and sagittal directions, respectively, over the active area of the mirror. The KB mirror system requires r.m.s. slope errors of 0.5 µrad (vertical) and 1.0 µrad (horizontal) with no more than 3 Å r.m.s. surface roughness. The mirror systems installed in the beamline met or exceeded these requirements.

The r.m.s. surface roughness of the vertical and horizontal KB mirrors over the active region was 2 Å with r.m.s. slope errors of 0.51 µrad and 0.79 µrad, respectively. It should be noted that horizontal focusing is dependent on the source size, which can be controlled by the manipulation of the secondary slits, and, while the horizontal beam size can be reduced in this manner, this is at the expense of beam flux.

In addition to the aforementioned optical elements, retractable filters/diagnostics are installed after each optical element. For the white beam section of the beamline, these consist of a water-cooled copper rod with a number of apertures into which diamond and pyrocarbon filters of different thickness are fitted. One of these on each rod is an optical quality diamond allowing visualization of the beam on an adjacent camera. The monochromatic diagnostics consist of a pair of sticks at each location with various metal foils (for energy calibration), aluminium foils of different thicknesses (for attenuation), Y_2O_3:Eu-coated Kapton screens and diodes fitted. The final diagnostic stick also has isolated nickel and gold grids and a 0.75 µm aluminium foil, which can be used in lower-energy experiments to record a drain current measurement of the beam intensity before the KB mirrors.

2.2. Instrumentation and control

The beamline uses a micro-ion chamber mic-r20 (Repic) to measure the incident beam intensity. This is normally used in flow mode with a helium flow rate of 50 sccm min^{-1} at atmospheric pressure. Most fluorescence detection is made using a nine-element monolithic germanium detector (Ortec). This is coupled to the XSPRESS-2 detector backplane, which was developed for Diamond by the Science and Technology Facilities Council (STFC) (Farrow *et al.*, 1995). This detector can be used for X-ray absorption spectroscopy measurements at count rates up to 150 kHz per channel using a dead-time correction. For X-ray energies below 4.5 keV, a four-channel silicon drift detector (SII NanoTechnology) has been installed, which is used in conjunction with an adapted standard glove bag filled with helium, that includes the I0 ion chamber, the sample and the detector. A large-area single XDI-VHR camera (Photonic Science) is used for collecting micro-diffraction images in transmission mode.

The sample is usually mounted on a holder plate which attaches to a kinematic mount, on a eight-axis sample stage (Newport). The stage has 100 nm repeatability in the directions in the sample plane. The same kinematic mount exists in our offline equipment, such as optical microscope and FT-IR microscope, so that regions of interest can be identified in the laboratory prior to XRF mapping. The sample mount is extremely flexible, allowing a range of sample types and customized holders to be fitted. We have designed and built a room-temperature electron yield cell and also have constructed an electron yield furnace that uses a battery-powered heater and controller to reduce electrical noise. This can heat materials to 573 K in a helium atmosphere. The beamline is also equipped with two Linkam microscope stages, HFSE91 and TS1500, for variable-temperature fluorescence work.

The majority of beamline components are controlled using *EPICS* (Dalesio *et al.*, 1994); the user interface is provided by the *Generic Data Acquisition* program (Gibbons, 2008). This is a Java-based application, common across the Diamond beamlines, which provides standard GUI interfaces for EXAFS and XRF mapping along with the ability to provide scripted bespoke solutions to non-standard experiments and user-supplied equipment.

2.3. Experimental performance compared with theoretical calculations

To date, the beamline has successfully provided microfocus beam across the intended operational range encompassing experiments from phosphorous (*K*-edge 2.145 keV) to molybdenum (*K*-edge 20.000 keV). This operational range can be achieved successfully owing to the small phase error of the undulator, which allows operation up to the 19th harmonic while maintaining a high photon flux at the sample. The flux at the sample at 10 keV is typically 2×10^{12} photons s^{-1}. A comparison between the measured and theoretical output of the undulator at 10 keV is shown in Fig. 2. The intensity was recorded at the sample position using a Si diode which was calibrated by an external metrology laboratory (Physikalisch-Technische Bundesanstalt). The measurements were taken with an unfocused beam owing to concerns over damage to the device and potential changes in performance with a focused beam. The theoretical output was calculated using the program *Spectra* (Tanaka & Kitamura, 2006), and is based on intensity after the first defining slit (S1 in Fig. 1). To compare the two outputs, corrections have to be made to the measurements at the sample position for sources of attenuation (air, Kapton windows) and the acceptance of the defining slits (S2, S3 in Fig. 1). In addition, undulator output is normally quoted in photons s^{-1} (0.1% energy bandpass)$^{-1}$ so a correction must also be made for the bandpass of the monochromator crystals, *i.e.* 0.014% for Si(111) crystals. The comparison shows that the intensity trend is well matched with no obvious fall-off at higher harmonics owing to the low phase

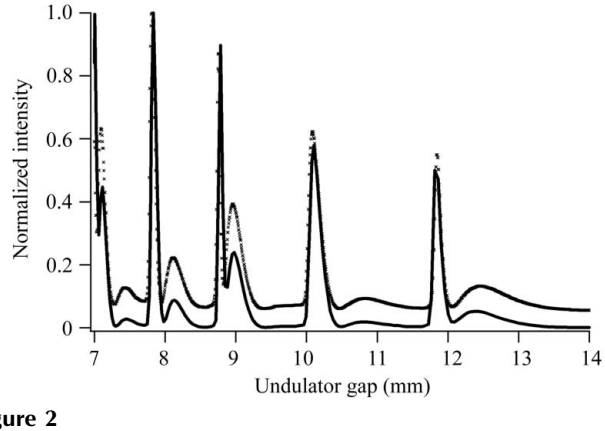

Figure 2
Comparison of the flux output spectrum recorded at 10 keV (solid line) with theoretical values (dotted line).

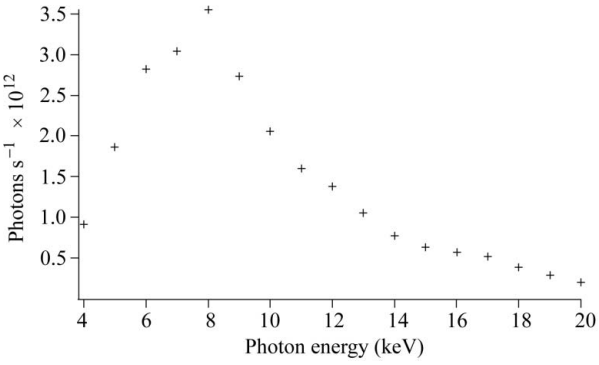

Figure 3
Photon flux of the beamline measured at the sample position from 4 to 20 keV.

error. The absolute intensities are not identical to the theoretical values; we believe this is due to uncertainties in the slit positions and slight misalignment at the time of measurement.

Fig. 3 shows the measured photon flux over the range 4–20 keV using the set-up previously outlined. The flux is at a maximum of 3.5×10^{12} photon s^{-1} at 8 keV. The measurements from 4 to 7 keV were made using the harmonic rejection mirrors, while for those from 8 to 20 keV the harmonic rejection mirrors are out of the beam. The beam size was such that it would have filled the optically active part of the KB mirrors if they were set to a 3 mrad incidence angle.

To measure the focal spot size, knife-edge scans using Au wire were used. The smallest FWHM spot size obtained so far at 10 keV is 2.1 × 2.5 μm (h × v). This larger than expected vertical beam size is primarily a result of beam movement; this is caused by vibrations of the monochromator second crystal. The mirrors are achromatic hence the focus should be independent of X-ray energy. An example of this is shown in Fig. 4, which shows a 3 μm beam profile at 4.5 and 13.2 keV. The profile is measured using a 200 μm gold wire that is scanned through the beam in 1 μm steps, with the intensity of the transmitted beam recorded on an ion chamber. A new crystal cage, holding a single-crystal set, has been designed to address this problem, including indirect cooling of the second crystal *via* copper braids; initial finite element analysis showed a considerable improvement in stability.

Focusing of the KB mirrors can be achieved using the interaction matrix approach outlined by Hignette *et al.* (1997). Initial operation of the bimorph mirrors found that using the interaction matrix approach a focus of at best 5–8 μm could be achieved. Accurate control of the shape of any mirror depends strongly on the reliability of the actuation process, whether it be mechanical or piezoelectric. The power supply used to control the bimorph was found to be of insufficient accuracy and reliability to focus the mirrors using a linear technique, and could not be replaced in a timely manner so an alternative method was therefore developed. With the mirror roughly focused, the beam width and shape were measured using knife-edge scans. An automated scheme based on the Nelder–Mead non-linear optimization algorithm was employed, which altered the mirror voltages with the aim of reducing the size of the beam (Nelder & Mead, 1965). This scheme, which may be

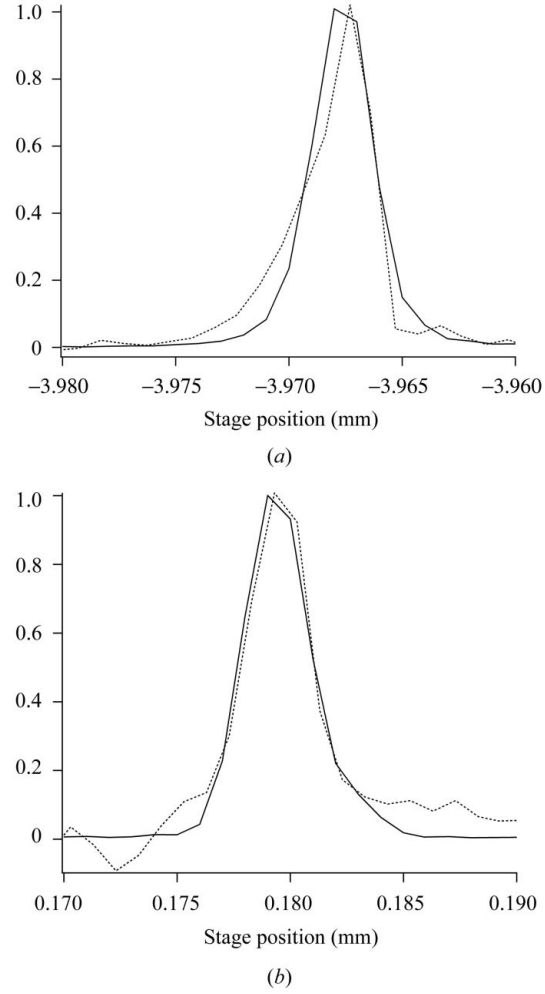

Figure 4
Vertical (*a*) and horizontal (*b*) 3 μm beam profiles measured at 4.5 keV (dotted line) and 13.2 keV (full line).

adapted to any system in which the actuation system is non-linear, enabled focusing down to 2.1 μm × 2.5 μm (h × v) FWHM at 10 keV.

3. Summary of early scientific results

3.1. Micro-XAFS study of the Santa Catharina meteorite

The Santa Catharina meteorite represents a natural invar system, and primarily comprises a taenite bulk host phase with a honeycomb network of oxide inclusions. It is of interest as it comprises equilibrium invar-type alloy phases that have been able to develop only because of the very slow cooling of the meteorite. Experimentally, these phases cannot be obtained owing to the extremely slow diffusion rates at low temperatures. Despite continued study over the last 20 years, there still remains a lack of understanding of the chemical, textural and morphological relationships between the various phases in the different and complex microstructural regions of the meteorite. In particular, there are four main phases in the meteorite: a bulk invar phase; nickel phosphide grains, typically 150 μm or so in size; a Ni-depleted metallic phase around the phosphide grains, which is about 30–50 μm thick; and a

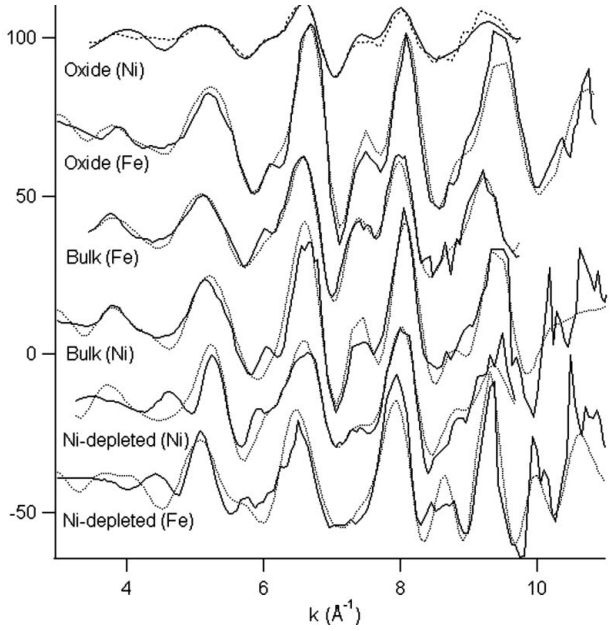

Figure 5
k^3-weighted EXAFS data (solid lines) from different regions within the Santa Catharina meteorite, plotted with their respective simulations (dotted lines). The spectra are from the oxide region (top), the bulk invar region (middle) and the Ni-depleted region (bottom).

rough oxidic phase, where there are small sub-10 µm grains in clusters. In order to look for subtle differences in the local structural environment of the Fe and Ni in these various phases, microfocus EXAFS data were collected in fluorescence mode from three different regions of the sample in fluorescence mode with a beam size of 4 × 4 µm (h × v). The EXAFS given in Fig. 5 shows fitted Ni and Fe *K*-edge data from the main bulk invar phase, the Ni-depleted Fe–Ni phase and the oxidic region. The EXAFS was reduced using the program *Athena* (Ravel & Newville, 2005), where a self-absorption correction was made and fitted in the program *DL-Excurv* (Tomic *et al.*, 2005). Characterization of the low-Ni metallic Fe–Ni phase, potentially antitaenite, suggests that the Fe and Ni are atomically disordered with respect to the bulk invar metal phase, and XANES (not shown) suggests that the Fe within these two metallic phases has different electronic structures. The EXAFS analysis supports the suggestion that the non-stoichiometric Fe_2NiO_4 is the main oxidic phase (Schofield *et al.*, 2009).

3.2. Transmission mapping of antidot assemblies

Highly ordered films of transition metals can be made by electrochemical deposition into the interstices between polystyrene latex spheres which have self-assembled on the surface of gold electrodes (Bartlett *et al.*, 2000). Washing away the polymer leaves a highly periodic hexagonal array of macropores with smooth curved surfaces, the diameter of which are determined by that of the latex particles (<100 nm) (Bartlett *et al.*, 2002). These materials can be grown to controlled and graded thicknesses. A wide variety of functional materials can be patterned into such antidot arrays, including magnetic and

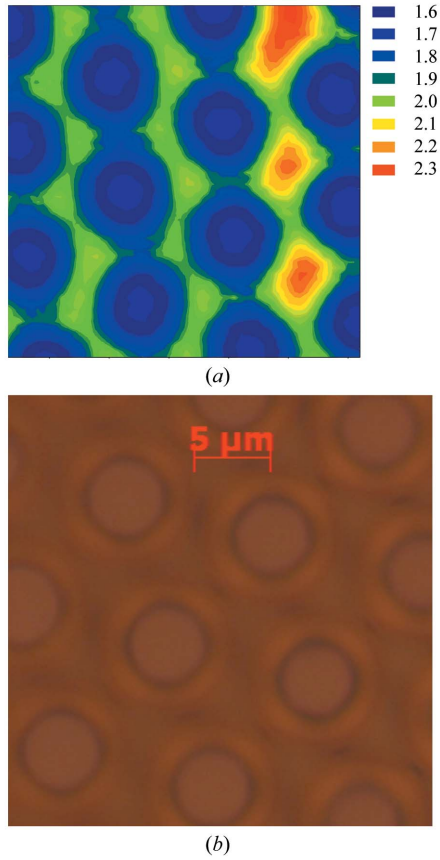

Figure 6
30 × 30 µm X-ray transmission map with a 1 µm pixel size (*a*) of an Au/Pt antidot array sample measured at 11600 eV, showing the platinum structure and optical image (*b*). The intensity scale represents the absorbance at each pixel.

superconducting metals (Coyle *et al.*, 2001). Micro-XAS has been applied to image the individual elements in these materials. Monometallic films and layered samples were investigated based upon Pt and Au. Polystyrene latex spheres with a diameter (*d*) of 10 µm were used as the template. Electroplating was applied with a metal layer thickness of ∼1/3 to ∼1/2 times the diameter *d*, imaging a series of open-cup structures. An Au–Pt–Au layered sample (with thickness = 0.4*d*) was synthesized in stages. The structures were imaged with Au and Pt L_3-edge XAS at excitation energies of 12.0 and 11.6 keV, respectively.

Images were obtained in transmission mode using a 3 × 4 µm (h × v) beam with a step size of 1 µm. Fig. 6 shows the Pt edge map for the layered sample compared with an optical micrograph. Possible alloying between the different elements was monitored by micro-XANES, which did not show any alloying between the metals for these materials. Further micro-XAS studies are planned on films that are covered with functional groups.

3.3. Titanium implant residue

Titanium and Ti-alloys are used extensively to manufacture biomedical prostheses for orthopaedic, oral and craniofacial rehabilitation. Titanium is largely biocompatible owing to the

presence of a passive oxide surface layer and as a consequence is associated with a largely predictable biological response following osseous implantation. However, under specific conditions, wear and corrosion processes result in the generation of titanium particles and the leaching of titanium ions into the surrounding tissues. Ti implant degradation *in vivo* will be highly dependent on the implant composition, geometry, mechanical loading and so forth. In order to produce realistic models for *in vitro* modelling of the impact of corrosion at the cellular and molecular level, information on the concentration and distribution of titanium ions encountered in periprosthetic soft tissue environments is required.

A sample of tissue from around a removed epithelial implant was cryo-tomed to a 10 µm slice and mounted on a high-purity quartz slide. It was sealed with a Kapton protective layer. X-ray fluorescence maps were used to identify the relative concentration and distribution. XANES was then conducted on a few representative regions to determine whether the local Ti environment varied as a function of concentration. Fig. 7 shows the micro-fluorescence map of the Ti concentration in epithelial tissue (200 × 55 µm). The data were recorded using the four-element Si drift detector and an excitation energy of 5.5 keV with a 4.5 µm beam. The corresponding XANES data (not shown) showed two distinct Ti environments. XANES spectra taken at high Ti concentrations showed a clear pre-peak indicating that metallic Ti is present, while spectra taken at low and intermediate concentrations showed no pre-peak and were representative of Ti in its oxide environment (six-fold coordinated). Larger-scale future studies are planned to explore the presence of Ti recovered from tissue surrounding a wide range of orthopaedic and dental implants, including different Ti alloys.

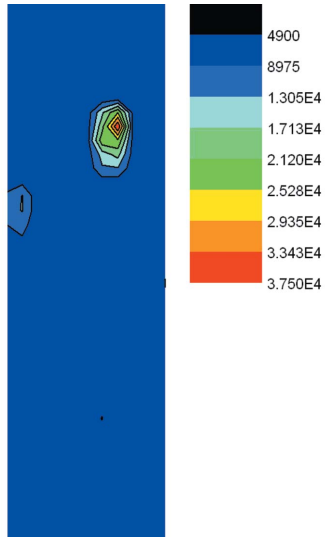

Figure 7
150 × 30 µm map of Ti fluorescence from epithetial tissue (200 × 55 µm with a 5 µm pixel size). The intensity scale represents the number of counts at each pixel.

4. Conclusion

The spectroscopy beamline at Diamond has now been operating for two years. In that time approximately 40 user experiments have taken place on the beamline. These experiments have covered a broad range of science from extra-terrestrial materials to human tissue samples, demonstrating the value of microfocus XAS in many fields. EXAFS data up to $k = 12$ Å^{-1} have been obtained from a wide range of samples, while the high flux has enabled XANES data to be collected on a sample with a concentration of Cr as low as 100 p.p.b. Improvements in the photon spot size are expected through a series of upgrades scheduled in the next year.

We thank Dr Paul Schofield (Natural History Museum), Dr Andy Smith (STFC) and Dr Caroline Kirk (Lougborough University) for permission to include the Santa Catherina data, Dr Owen Addison (University of Birmingham) for permission to include the Ti implant data and Professor John Evans and Dr Moniek Tromp (University of Southampton) for permission to include the antidots data. We would like to express our gratitude to the beamline user working group and all the staff at Diamond and STFC who have contributed to the construction and commissioning of the beamline. We thank two anonymous referees for their constructive criticism.

References

Bartlett, P. N., Baumberg, J. J., Birkin, P. R., Ghanem, M. A. & Netti, M. C. (2002). *Chem. Mater.* **14**, 2199–2208.
Bartlett, P. N., Birkin, P. R. & Ghanem, M. A. (2000). *Chem. Commun.* pp. 1671–1672.
Coyle, S., Netti, M. C., Baumberg, J. J., Ghanem, M. A., Birkin, P. R., Bartlett, P. A. & Whittaker, D. M. (2001). *Phys. Rev. Lett.* **87**, 176801.
Dalesio, L. R., Hill, J. O., Kraimer, M., Lewis, S., Murray, D., Hunt, S., Watson, W., Clausen, M. & Dalesio, J. (1994). *Nucl. Instrum. Methods Phys. Res. A*, **352**, 179–184.
Evans, J. (2006). *Phys. Chem. Chem. Phys.* **8**, 3045–3058.
Farrow, R., Derbyshire, G. E., Dobson, B. R., Dent, A. J., Bogg, D., Headspith, J., Lawton, R., Martini, M. & Buxton, K. (1995). *Nucl. Instrum. Methods Phys. Res. B*, **97**, 567–571.
Flank, A.-M., Cauchon, G., Lagarde, P., Bac, S., Janousch, M., Wetter, R., Dubuisson, J.-M., Idir, M., Langlois, F., Moreno, T. & Vantelon, D. (2006). *Nucl. Instrum. Methods Phys. Res. B*, **246**, 269–274.
Gibbons, P. (2008). *NOBUGS 2008 Conference*, ANSTO, Australia (http://www.nbi.ansto.gov.au/cgi-bin/nobugs2008/abstractView.ws3?abfile=abstract159.txt).
Hignette, O., Freund, A. & Chinchio, E. (1997). *Proc. SPIE*, **3152**, 112–119.
Kemner, K. M. (2008). *Geobiology*, **6**, 270–277.
Kirkpatrick, P. & Baez, A. Z. (1948). *J. Opt. Soc. Am.* **38**, 766–774.
Nelder, J. A. & Mead, R. (1965). *Comput. J.* **7**, 308–313.
Ravel, B. & Newville, M. (2005). *J. Synchrotron Rad.* **12**, 537–541.
Scheidegger, A. M.,. Vespa, M., Grolimund, D., Wieland, E., Harfouche, M., Bonhoure, I. & Dähn, R. (2006). *Waste Manage.* **26**, 699–705.
Schofield, P., Smith, A., Mosselmans, F., Scholl, A., Anders, S., Cressey, G., Cressey, B., Quinn, P., Kirk, C. & Hogg, S. (2009). *Geostand. Geoanal. Res.* Accepted.
Signorato, R., Hignette, O. & Goulon, J. (1998). *J. Synchrotron Rad.* **5**, 797–800.

Susini, J., Labergerie, D. & Hignette, O. (1996). *Proc. SPIE*, **2856**, 130–144.
Susini, J., Labergerie, D. & Zhang, L. (1995). *Rev. Sci. Instrum.* **66**, 2229–2231.
Tanaka, T. & Kitamura, H. (2006). *SPECTRA – A Synchrotron Radiation Calculation Code*, http://radiant.harima.riken.go.jp/spectra/.
Tomic, S., Searle, B. G., Wander, A., Harrison, N. M., Dent, A. J., Mosselmans, J. F. W. & Inglesfield, J. E. (2005). *The DL_EXCURV Package.* CCLRC Technical Report DL-TR-2005–001.
Walker, R. & Fletcher, S. (2007). *Synchrotron Radiat. News*, **20**, 43–48.
Welnak, C., Chen, G. J. & Cerrina, F. (1994). *Nucl. Instrum. Methods Phys. Res. A*, **347**, 344–347.